*Special Issue on Metamaterials LHM*

# Efficient FDTD method for analysis of mushroom-structure based left-handed materials

W.-Y. Wu, A. Lai, C.-W. Kuo, K.M.K.H. Leong and T. Itoh

**Abstract:** A finite-difference time-domain method, combined with thin-wire and thin-slot algorithms, which is used to analyse a metamaterial based on periodic mushroom structures, is proposed. This proposed method is suitable for analysing problems involving large structures with fine structural details. Several composite right/left handed (CRLH) metamaterial mushroom-based structures are investigated. A $19 \times 8$ flat lens and a parabolic lens structure composed of 410 unit mushroom cells are investigated and they demonstrate negative-refractive-index characteristics while operating in the LH region. The simulation and measurement results of one- and two-dimensional CRLH mushroom-based structures are compared. The periodic analysis for mushroom structures is also introduced. Only a single unit mushroom cell is required to present the phenomena of infinite periodicity with periodic boundary conditions.

## 1 Introduction

The main characteristics of left-handed material (LHM) [1] are negative permeability and permittivity ($\mu < 0$, $\varepsilon < 0$) simultaneously; thus the direction of phase propagation and the direction of the Poynting vector are anti-parallel. An LHM is also called negative-refractive-index (NRI) medium and not commonly found in nature. Accordingly, this material is often realised using periodic structures with unit-cells designed to provide LHM characteristics. The periodic structure based on mushroom-like unit cells is one example of an LHM [2–7]. It consists of a periodic arrangement of square metal patches each connected by a via from the centre of the patch to the ground plane. These mushroom-like structures have been shown to behave as composite right/left handed (CRLH) metamaterials, and exhibit LH properties at low frequencies and right-handed (RH) properties at high frequencies. Because this type of LHM is based on periodicity, it is most common to analyse it using periodic structure analysis methods. Since these methods assume the existence of an infinite structure, details such as interfacing with other media and mode excitation are difficult to explore. Therefore examination of a finite structure may prove necessary. LHM structures are often designed having a unit cell which is considerably small in terms of wavelength but a large collection of unit cells must be examined to see the total LHM effect. This presents a difficulty in performing full-wave analysis of LHM structures.

Several researchers have proposed several methods to analyse complex CRLH structures, for example equivalent circuit method [3, 8], transmission-line theory [7] or effective media method [4, 9, 10]. All of these methods rely on circuit models and approximations of the structure rather than the full structure itself. This is done to save computational time and resources. In this paper, we combine the finite-difference time-domain method (FDTD) [11] with thin wire [12, 13] and thin-slot techniques [14, 15] to simulate mushroom structures. The motivation for using the FDTD method to model the mushroom structures is that the transient behaviours of the structure can be straightforwardly obtained. For structures simulated in this paper, a huge computational resource is required if uniform discretisation is applied throughout the whole computational domain without any approximation. Non-uniform gridding may alleviate this problem with the caveat that the largest and smallest grid sizes should not differ too much, because strong spurious reflection might occur between adjacent grids of different sizes. The advantage of our approach is that the spatial increments ($\Delta x$, $\Delta y$, $\Delta z$) are not limited to the minimum structural details of the simulated structures, and consequently the computational resources can be saved greatly. This paper will discuss the proposed FDTD analysis method as well as provide some comparisons between this simulation method and measured results.

## 2 Explanation of FDTD algorithm for analysis of 1D linear four-cell mushroom structure

Since Yee's FDTD method is an explicit time stepping scheme, restricted by the Courant–Friedrich–Levy (CFL) stability condition [12]. Accordingly, very fine spatial and temporal increments are required when the method is applied to problems with very fine structural details that are a small fraction of the shortest wavelength within the frequency band of interest. Using these very fine spatial and temporal increments leads to excessively large number of time steps and mesh grids, which in turn lengthens the computation time. The spatial increments in our proposed FDTD method are not limited to the minimum structural details of the simulated structures due to the use of thin wire and thin-slot algorithms; thus the computer burden can be reduced by increasing the value of spatial increments. Although enlarging spatial increments will increase the numerical dispersion error,



doi:10.1049/iet-map:20050230

Paper first received 28th September and in revised form 25th December 2005

W.-Y. Wu and C.-W. Kuo are with the Department of Electrical Engineering, National Sun Yat-sen University, 70 Lien-hai Rd., Kaohsiung 804, Taiwan

A. Lai, K.M.K.H. Leong and T. Itoh are with the Department of Electrical Engineering, University of California, Los Angeles, 405 Hilgard Ave., Los Angeles, CA, 90095 USA

E-mail: wywu@ucla.edu

usage of computer memory and simulation time are reduced greatly.

For example in the 2D case, if $\Delta x$ and $\Delta y$ are doubled, then the consumption of computer memory reduces to $1/4$ and $\Delta t$ can be increased by a factor of two due to the looser restriction of stability criterion. The overall effect of the increase of $\Delta x$ and $\Delta y$ is an acceleration of the simulation speed to eight times. Therefore huge periodic structures can be simulated more efficiently, and the choice of spatial increment depends only on acceptable dispersion error, not the minimum size of the simulated structures.

The LHM structures considered in this paper are based on 1D or 2D lattices of mushroom structure unit cells. Fig. 1 shows a 1D linear four-cell mushroom structure connected with two short microstrip lines as the input/output ports. In Fig. 1, the coupling of the top patch to the adjacent patches provides the LH capacitance, whereas the via connecting the top patch to the ground plane provides the LH inductance. The gap width and via radius are very small compared to the size of the unit mushroom. Given these conditions, the thin-wire and thin-slot algorithms are incorporated into the FDTD method to avoid discretisation of fine structural details and to save computational time.

The thin wire algorithm [12] is based on quasi-static assumption of the field distributions. If there is a thin wire placed along $z$-direction and the radius of the thin wire is very smaller than FDTD spatial increment ($\Delta x$ or $\Delta y$), general discretisation method is hard to model this problem. A quasi-static assumption assumes that the looping magnetic and radial electric fields nearest to the wire vary with $1/r$, where $r$ is the radial distance from the centre of the wire. In this approach, only the FDTD updating equations of looping magnetic components immediately adjacent to the wire need to be modified. According to Faraday's law, the FDTD updating equation of $H_y$ component immediately adjacent to the wire can be derived as

$$H_y\Big|_{i+1/2,j,k+1/2}^{n+1/2} = H_y\Big|_{i+1/2,j,k+1/2}^{n-1/2} - \frac{\Delta t}{\mu}\left[\frac{E_x|_{i+1/2,j,k+1}^{n} - E_x|_{i+1/2,j,k}^{n}}{\Delta z} - \frac{E_z|_{i+1,j,k+1/2}^{n}}{\Delta x/2 \cdot \ln(\Delta x/a)}\right] \quad (1)$$

where $a$ is the radius of the wire; $i$, $j$, $k$ are the coordinate indexes of the wire; $k$ may vary with the length of wire. Other three looping $H$ components also must be modified.

The thin-slot algorithm is proposed by Gilbert and Holland [14]. This algorithm approximates the thin-slot effect by calculating the effective capacitance between two adjacent PEC plates. According to Gkatzianas *et al.* [15], the in-cell capacitance is evaluated as

$$C_{\text{in-cell}} = \frac{2\varepsilon_0}{\pi}\ln\left[\frac{\Delta}{2w} + \sqrt{\left(\frac{\Delta}{2w}\right)^2 - 1}\right] \quad (2)$$

where $\Delta$ is the spatial increment which is parallel to PEC plates and perpendicular to thin-slot; $w$ is half the width of the thin-slot. The effective relative permittivity derived from the in-cell capacitance is given by

$$\varepsilon_{r,\text{eff}} = 1 + \frac{C_{\text{in-cell}}}{\varepsilon_0} \quad (3)$$

This approach is one of the simplest and most efficient thin-slot models for FDTD applications. It straightforwardly replaces original medium by effective medium to approximate the thin-slot effect.

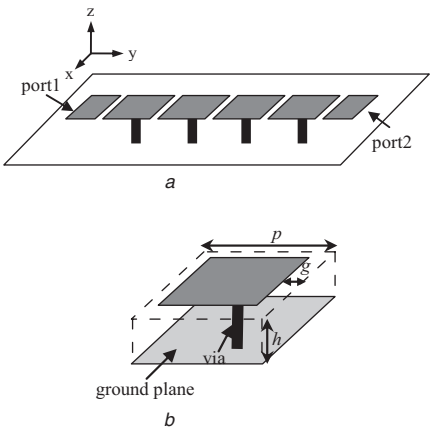


**Fig. 1** *Mushroom structure*

*a* Linear four-cell unit
*b* A unit cell
$p = 5$ mm, $g = 0.1$ mm, $h = 1.27$ mm, via radius $= 0.12$ mm, $\varepsilon_r = 10.2$

The two algorithms mentioned earlier are not used for applications which require high accuracy. Their main purpose is to provide acceptable answers with large computational savings. For the linear four-cell mushroom structure case, at least 50 grids per unit cell along the $y$-direction are required if uniform discretisation is employed. In our simulation, only 9 grids are used to discretise a unit mushroom cell. Comparisons of the numerical and measurement data for the $S$-parameters are shown in Fig. 2.

Notice that the highest frequency of our simulation is 10 GHz which corresponds to a shortest wavelength

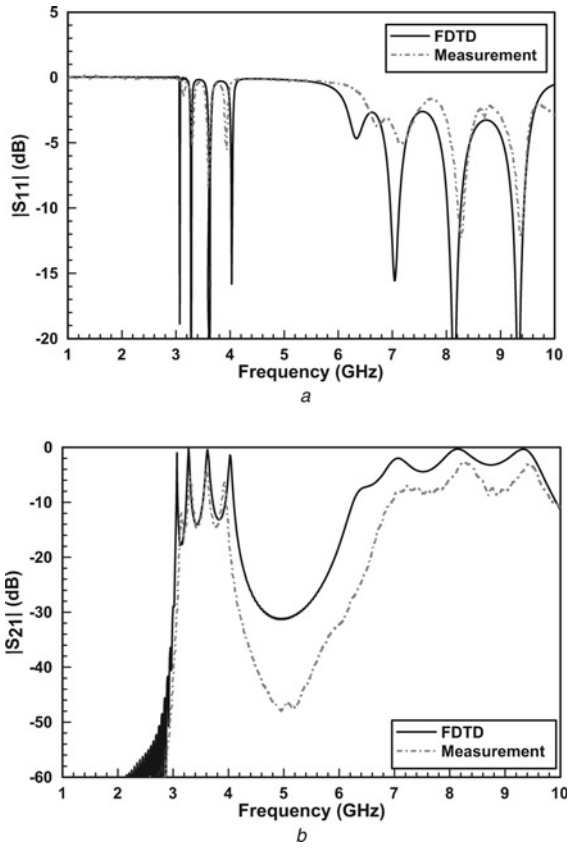


**Fig. 2** *S-parameter of the mushroom structure of Fig. 1*

*a* $S_{11}$
*b* $S_{21}$

($\lambda_{min}$) of 3 cm. The size of the spatial increments ($\Delta x$, $\Delta y$) is chosen to be $\lambda_{min}/54$, thus providing very good accuracy [16]; the temporal increments ($\Delta t$) is chosen to satisfy the FDTD stability condition. A wideband Gaussian pulse is applied to be the waveform of excitation source. It was determined that 50 thousand time steps are required to obtain a smooth frequency response since the magnitude of time-domain response becomes very small at later time steps and can be ignored in the calculation of the Fourier transformation. Perfectly matched layer (PML) [17] absorbing boundary conditions (ABCs) are used to absorb the radiation fields and simulate open space. In Fig. 2, the lowest four resonance frequencies belong to the LH region; the next four higher resonance frequencies belong to the RH region. The simulation and measurement results show similar trend and each resonance frequency matches well. Nevertheless, the conductor and dielectric losses are not considered in FDTD simulations, which may be the reason of magnitude difference between the results of simulation and measurement.

## 3 Calculation of dispersion diagram for mushroom structure LHM

### 3.1 Dispersion diagram calculation using periodic boundary condition

FDTD method used to analyse periodic structures, for example frequency selective surfaces (FSSs), can be performed well by the technique of periodic boundary conditions (PBCs) in the time domain formulation, since utilising PBCs to model periodic structures only needs to discretise and simulate one single unit cell [18, 19]. For this reason, use of the thin-wire and thin-slot algorithms is not necessary in this PBCs' simulation. In this section, a phase shift PBC based on Floquet theory incorporated with FDTD is proposed to obtain the mushroom structure's dispersion diagram. According to the 1D Floquet theory

$$\varphi(x, y + y_p, z) = \varphi(x, y, z) \exp(-jk_y \cdot y_p) \tag{4}$$

where $\varphi$ can be any electric or magnetic fields; $y_p$ is the length of unit period in $y$-axis; $k_y$ is propagation constant in $y$-axis.

Equation (4) is also illustrated with Fig. 3. In Fig. 3, there are two PBCs placed at $y = 0$ and $y = y_p$, respectively. The field components along each PBC differ only by a phase-shift term $\exp(-jk_y \cdot y_p)$, which makes all field components in FDTD a complex number. The FDTD updating equations

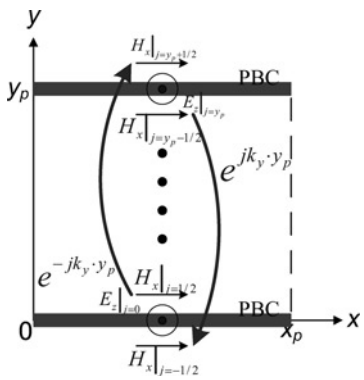


**Fig. 3** *Illustration of PBC*

near the PBC at $y = 0$ should be modified to

$$\varepsilon \frac{\partial E_z}{\partial t}\bigg|_{i,j=0} = \left( \frac{H_y\big|_{i+1/2,j=0}^{n+1/2} - H_y\big|_{i-1/2,j=0}^{n+1/2}}{\Delta x} - \frac{H_x\big|_{i,j=1/2}^{n+1/2} + H_x\big|_{i,j=-1/2}^{n+1/2}}{\Delta y} \right) \tag{5}$$

$$\begin{aligned} H_x\big|_{j=-1/2} &= H_x\big|_{j=y_p-1/2} \times \mathrm{e}^{jk_y \cdot y_p} \\ &= H_{xc}\big|_{j=y_p-1/2} \cdot \cos(k_y \cdot y_p) \\ &\quad - H_{xs}\big|_{y_p-1/2} \cdot \sin(k_y \cdot y_p) \\ &\quad + j[H_{xs}\big|_{y_p-1/2} \cdot \cos(k_y \cdot y_p) \\ &\quad + H_{xc}\big|_{y_p-1/2} \cdot \sin(k_y \cdot y_p)] \end{aligned} \tag{6}$$

where $H_{xc}$ is the real part of $H_x$, and $H_{xs}$ is the imaginary part of $H_x$. By the similar calculation, the FDTD updating equations near PBC at $y = y_p$ are

$$\varepsilon \frac{\partial E_z}{\partial t}\bigg|_{i,j=y_p} = \left( \frac{H_y\big|_{i+1/2,j=y_p}^{n+1/2} - H_y\big|_{i-1/2,j=y_p}^{n+1/2}}{\Delta x} - \frac{H_x\big|_{i,j=y_p+1/2}^{n+1/2} + H_x\big|_{i,j=y_p-1/2}^{n+1/2}}{\Delta y} \right) \tag{7}$$

$$\begin{aligned} H_x\big|_{j=y_p+1/2} &= H_x\big|_{j=1/2} \times \mathrm{e}^{-jk_y \cdot y_p} \\ &= H_{xc}\big|_{j=1/2} \cdot \cos(k_y \cdot y_p) \\ &\quad + H_{xs}\big|_{j=1/2} \cdot \sin(k_y \cdot y_p) \\ &\quad + j[H_{xs}\big|_{j=1/2} \cdot \cos(k_y \cdot y_p) \\ &\quad - H_{xc}\big|_{j=1/2} \cdot \sin(k_y \cdot y_p)]. \end{aligned} \tag{8}$$

In this work, all field components are limited to be real numbers; the sine/cosine method is therefore applied to split all field components into real and imaginary parts and then calculated, respectively. On the basis of this method, two separate simulation spaces with $\sin(\omega t)$ and $\cos(\omega t)$ time dependence excitations are used, moreover, the PBCs of these two spaces are related. While PBCs are placed at $x = 0$ and $x = x_p$, the updating equations can be also obtained in the same manner.

Fig. 4 shows a 3D unit-cell mushroom structure for periodic analysis. In Fig. 4*a*, two pairs of PBCs surround a square patch placed on the $x$—$y$ plane. In Fig. 4*b*, a square wire is placed along the $z$-direction and then connected to the centre of patch and the ground plane; a PML is used to terminate the open space in the top $z$-direction. An $E_z$ component is excited inside the substrate; a wideband Gaussian pulse multiplied by $\sin(\omega t)$ and $\cos(\omega t)$ time harmonic functions is used to be the excitation waveform in the simulation spaces of real and imaginary parts, respectively. An observation point is chosen to record time-domain field response and then transform to frequency-domain response by Fourier's transformation. The electromagnetic (EM) wave reflection and transmission behaviours in periodical arrangement structures are caused by the PBCs; this simulation therefore requires only one

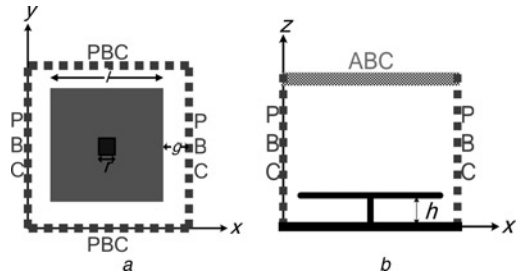


**Fig. 4** *Unit cell mushroom structure for periodic analysis*
*a* Top view
*b* Side view
$l$ = 4.8 mm, $g$ = 0.1 mm, $h$ = 1.27 mm, $r$ = 0.24 mm, $\varepsilon_r$ = 10.2

unit-cell of periodic structures to perform infinite periodicity. While a wideband input signal is used, only the energy corresponding to the frequencies of propagation modes can survive in PBCs' simulation, however, the energy corresponding to other frequencies decays very fast. The values of PBCs' propagation constants $k_x$ and $k_y$ to indicate certain point on the axis of the Brillouin diagram are chosen, and then the resonant frequencies corresponding to the different propagation modes can be observed from the frequency-domain response of the observation point. By changing the value of propagation constants continuously, the resonant modes are recorded and represented in Fig. 5. In Fig. 5, the $\Gamma$, $X$ and $M$ represent the points ($k_x$ $x_p = k_y$ $y_p = 0$), ($k_x$ $x_p = \pi$, $k_y$ $y_p = 0$) and ($k_x$ $x_p = k_y$ $y_p = \pi$), respectively. The circular symbols (LH) in Fig. 5 show that the mushroom structure supports a backward wave, since the sign of $v_p$ and $v_g$ are opposite. Moreover, the diamond symbols (RH) show a forward wave due to the same sign of $v_p$ and $v_g$. In the frequency range between LH and RH region, $\beta$ becomes imaginary, and therefore a stopband is present. Where $\beta$ is small enough, the LH mode will couple to the air mode, and also the EM wave is no longer concentrated in the substrate.

### 3.2 Dispersion diagram calculation using S-parameters

The extraction of the $S$-parameters of the structure can be directly used in the calculation of the structure's dispersion characteristics. The Brillouin diagram from $\Gamma$ to $X$ can be obtained by calculating the propagation constant of an infinite structure along one of the principle axis ($x$ or $y$ for isotropic structure). This is done by using a 1D four-cell row of mushroom structures and using perfectly magnetic conductor (PMC) walls placed along both sides of the row of unit cells. This is equivalent to a structure with infinite number

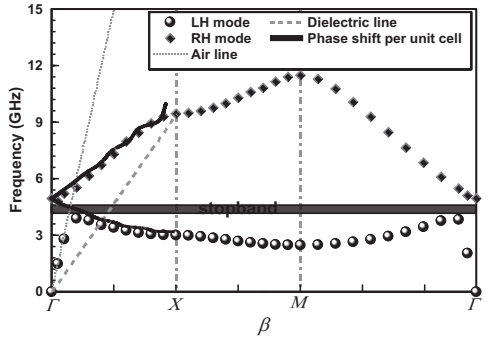


**Fig. 5** *Dispersion diagram of mushroom structure calculated by PBCs*

of unit cells in the $x$-direction, with $k_x = 0$. By finding the propagation constant in the $y$-direction, the Brillouin diagram from $\Gamma$ to $X$ can be obtained. Two PMCs are spaced out 5 mm apart to preserve 2D symmetry and placed at both sides of the 1D linear four-cell mushroom structure along the $y$-direction. To simplify this simulation, the input and output microstrip lines are assumed very small and well impedance matched; the reflection wave is therefore ignored in the following calculation. The incident voltage in port1 and the voltage in port2 can be written as

$$v_{inc}(f) = V_{inc}(f)e^{-j\beta(f)y_S} \tag{9a}$$

$$v_L(f) = V_L(f)e^{-j\beta(f)y_L} \tag{9b}$$

where $\beta(f)$ is the propagation constant of CRLH transmission line; $y_S$ and $y_L$ are the location of port1 and port2.

The Brillouin diagram form $\Gamma$ to $X$ can be regarded as a phase shift from one side of the unit cell to another side. The phase of $S_{21}$ already contains the phase shift from port1 to port2, which can be obtained as

$$S_{21} = \frac{v_L(f)}{v_{inc}(f)} = |S_{21}|e^{-j\beta(f)\cdot(y_L - y_S)} = |S_{21}|e^{-j\beta(f)\cdot(4p+2l)} \tag{10}$$

where $p$ is the length of a unit mushroom cell, and $l$ is the length of the microstrip line connected to the input and output of mushroom structure. The length $l$ should be small enough to not greatly interfere with the CRLH mode. The phase shift of a unit cell is derived as

$$\text{Phase}|_{\text{Unitcell}} = \frac{\left[\text{Phase}\left(S_{21}\big|_{\text{whole circuit}}\right) - \text{Phase}\left(S_{21}\big|_{\text{MSL}}\right)\right]}{4} \tag{11}$$

The solid line of dispersion diagram in Fig. 5 plots the result from the phase of $S$-parameter. The thin-wire and thin-slot algorithms are applied to simulate this structure. This result can be used to verify with PBCs' result and shows a good agreement. The direct calculation of phase shift indicates an easy and fast way to obtain a dispersion diagram from $\Gamma$ to $X$. It is worth noting that the results calculated from the phase of $S$-parameter present the propagation characteristic of traveling wave inside the planar circuit, but do not exhibit air line coupling because of a single mode (single $\beta$) assumption. For the frequency region of LH, the LH mode is much stronger than the air mode inside the substrate, only the LH mode can therefore be observed.

## 4 17 by 17-cell square mushroom structure

Although study of infinite 2D LHMs is important, simulation of a finite size structure is also essential. FDTD combined with thin-wire and thin-slot techniques can calculate mushroom structures very efficiently, especially for 2D structures. To demonstrate this concept, the measured and simulated results showing input impedance and near-field phase are compared. Fig. 6 shows a fabricated LHM using 17 by 17-cell mushroom structures. The centre mushroom is fed with a coaxial line. For analysis using FDTD, each mushroom cell is discretised to a 9 × 9 grid in FDTD. The size of $\Delta x$ and $\Delta y$ is $\lambda_{min}/54$ for the highest frequency (10 GHz); the size of $\Delta z$ is a quarter thickness of the substrate. A total of 154 × 154 × 16 FDTD grids have been used, and 150 thousand time steps are required for stable frequency responses. All calculations in this paper are

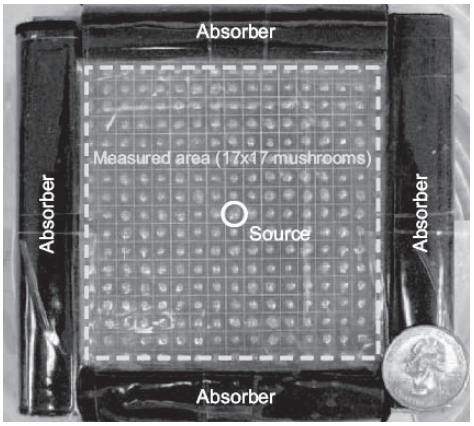


**Fig. 6** *17 by 17-cell square mushroom structure*

done on 2.4-GHz Intel Pentium 4 CPU. Nine hours is required for running this simulation.

The comparison of the $S_{11}$-parameter of the 17 by 17-cell mushroom structure is shown in Fig. 7. The $S_{11}$ results of simulation and measurement show similar trend when the mushroom structure is extended from one dimension to two dimensions. Differences may occur due to fabrication imperfections and imperfections of the absorbing material used to terminate the test structure. Near-field measurements were done using the experimental measurement setup shown in Fig. 8. A vertically oriented probe controlled by a mechanical stage and an Agilent 8510C network analyser is used to measure the electric field 2.0 mm atop the structure. Figs. 9 and 10 show the phase of the simulated and measured electric-field distributions, respectively. Four frequencies were chosen in the LH region, and similar phase patterns between simulation and measurement can be observed. By increasing the operational frequency, the wavelength of the electric field also increases because of the LH characteristics shown in Fig. 5. By applying the proposed algorithm to this 17 by 17 mushroom structure, the computation time speeds up about 90 times (spatial requirement reduces 25 times, and temporal requirement reduces 3.6 times) compared with that using only uniform discretisation.

## 5 Modeling of LH lenses

### 5.1 Interface between RH and LH mediums

Due to the NRI characteristics of the LHM, the EM waves travelling through the interface between an LHM and a

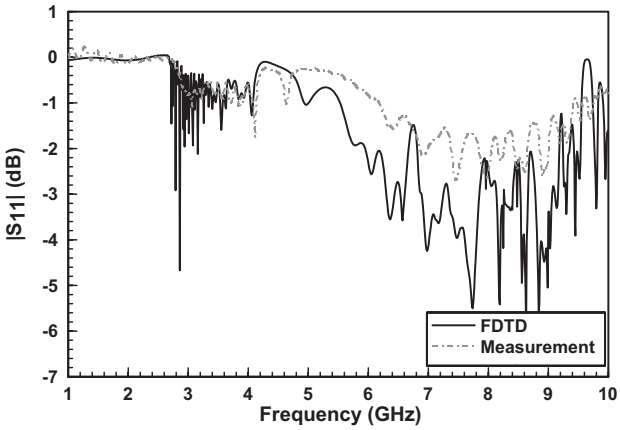


**Fig. 7** *S-parameter of the mushroom structure of Fig. 6*

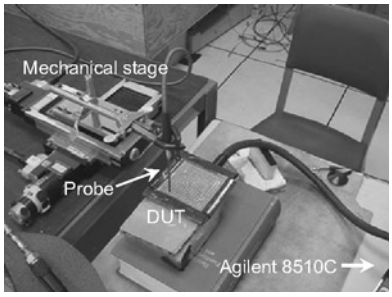


**Fig. 8** *Measurement setup of Fig. 6*

right-handed material (RHM) having positive refractive index will experience reversal of Snell's law. Therefore a concave RHM-based lens diverges radiation whereas a concave LHM-based lens converges radiation when interfaced with an RH region. The interface between LH and RH mediums is required to be conic (parabolic, elliptic or hyperbolic) to converge or diverge EM waves. This conic interface can be obtained by optical path length technique [20]. In the case of an NRI medium, a parabolic interface is required to focus a planar wave. In addition, a flat interface is able to refocus a point source for an NRI medium as a direct result of Snell's law. The advantage of LHM-based lenses is that the LH medium can be matched with the RH medium while $-n_{LH} = n_{RH}$; thus all incident EM waves are allowed to pass through the LH/RH interface without reflections. In this section, the CRLH mushroom structures are used to construct the LHM-based lenses, and then the RH/LH matching method can be realised by the dispersion diagram of Fig. 5. In Fig. 5, the cross point of two curves (LH mode and dielectric line) expresses that the RH/LH interface is phase-matched and occurs around 3.6 GHz. At this phase-matched operation, the RH region has a refractive index of 3.2, whereas the CRLH region has a refractive index of $-3.2$. A flat lens and a

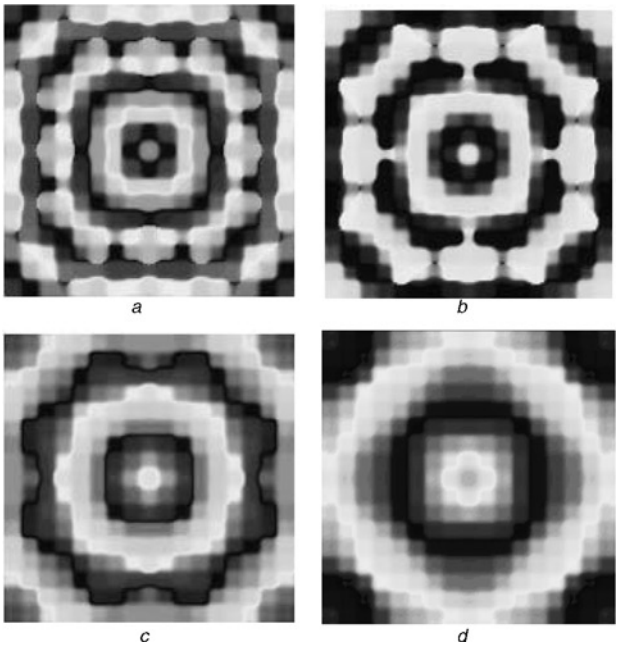


**Fig. 9** *FDTD simulation results of E-Field distribution of a 17 by 17 mushroom structure*

*a* 3.35 GHz
*b* 3.5 GHz
*c* 3.7 GHz
*d* 3.9 GHz

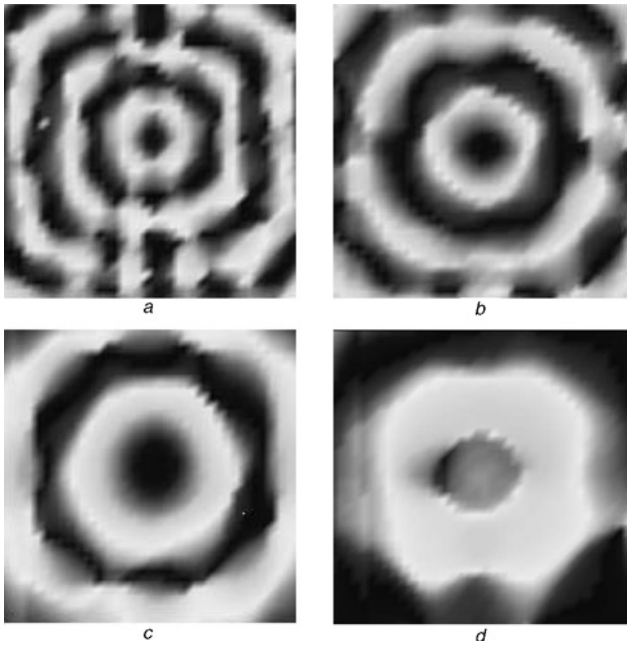


**Fig. 10** *Measurement results of E-Field distribution of a 17 by 17 mushroom structure*

*a* 3.35 GHz
*b* 3.5 GHz
*c* 3.7 GHz
*d* 3.9 GHz

parabolic lens consisting of mushroom structures are studied in the next sections.

### 5.2 Flat lens

The proposed FDTD method is used to simulate a flat LHM/RHM lens. Fig. 11 shows the schematic of the flat LHM-based lens, which is placed between two parallel plate waveguides (PPWs) and consists of 8 by 19 mushroom-structure unit cells. An excitation line source is placed inside the PPW and 20 mm away from the flat lens interface. Each mushroom cell and material is chosen to have the same value as the previous cases. A total of $172 \times 163 \times 12$ FDTD grids have been used, and 150 thousand time steps are required for stable frequency responses. The complex frequency shifted (CFS) [21, 22] PML is necessary to be applied in this complex case because the CFS-PML can absorb evanescent waves efficiently with long time signatures. Fig. 12 is the $E_z$ ($z$ is the vertical direction) field distribution inside the substrate in the frequency domain. Focusing is observed at 3.68 GHz, which is close to the expected focusing frequency of 3.6 GHz. As shown in

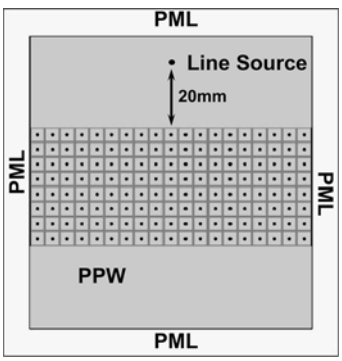


**Fig. 11** *Flat lens*

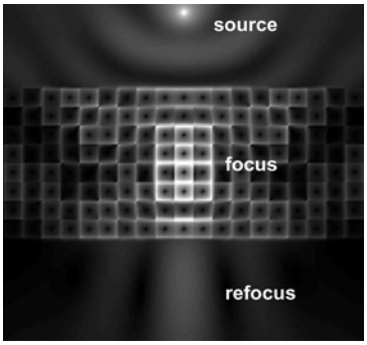


**Fig. 12** *$E_z$-field distribution of flat lens*

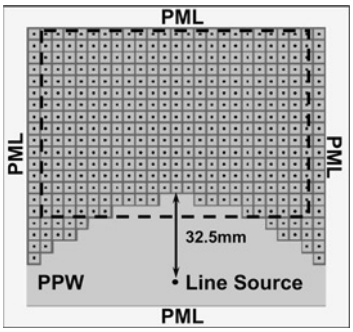


**Fig. 13** *Parabolic lens*

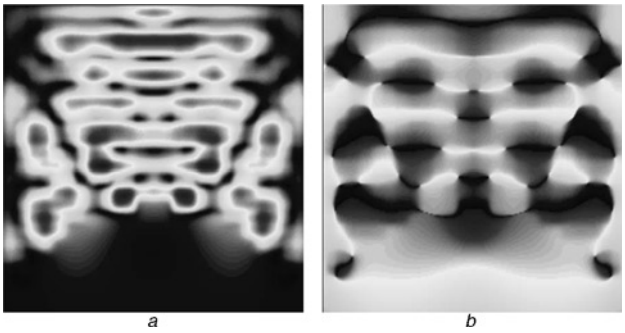


**Fig. 14** *FDTD simulations*

*a* *E*-field magnitude
*b* *E*-field phase

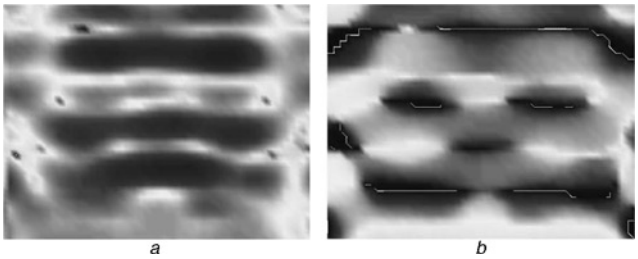


**Fig. 15** *Measurements*

*a* *E*-field magnitude
*b* *E*-field phase

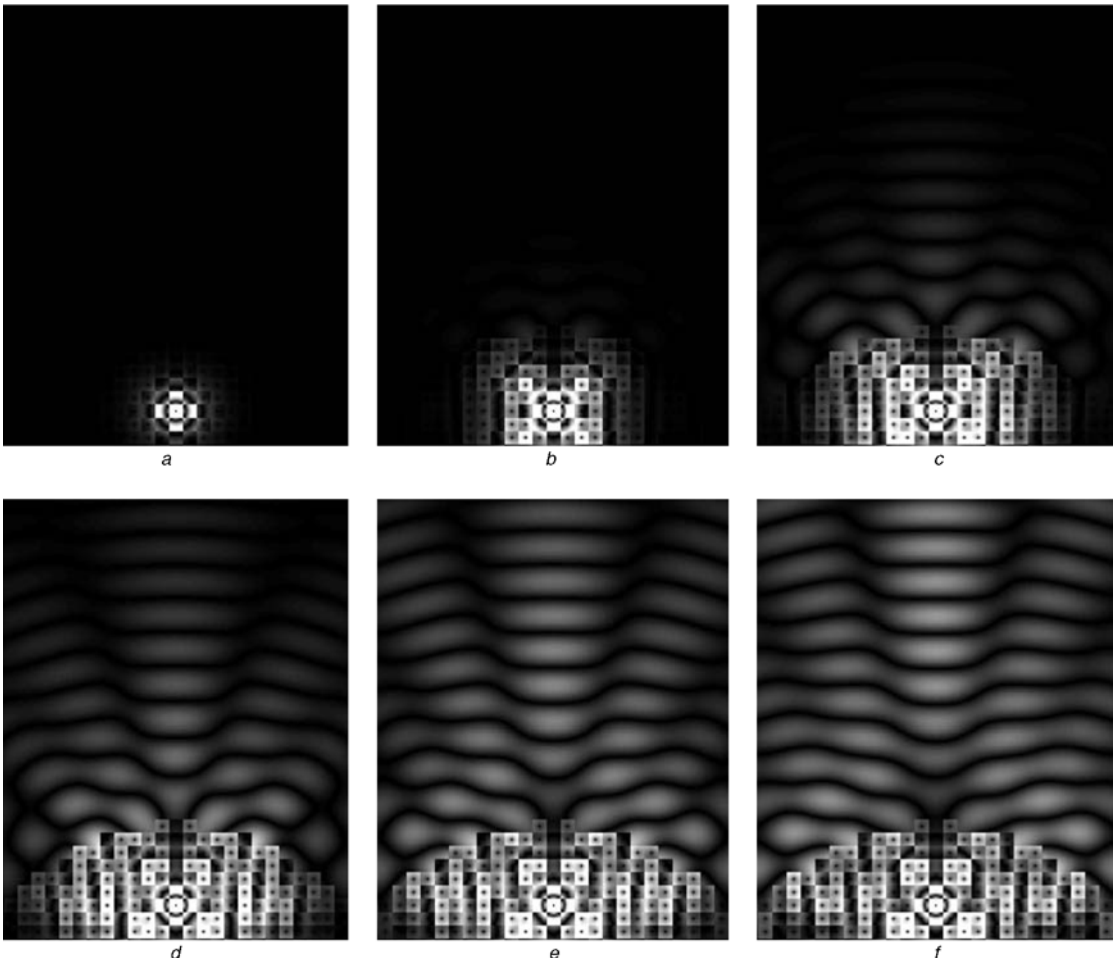


**Fig. 16** *Time-domain $E_z$-field distribution of parabolic lens*

*a* Time steps = 1000
*b* Time steps = 2000
*c* Time steps = 3000
*d* Time steps = 4000
*e* Time steps = 5000
*f* Time steps = 6000

Fig. 12, high field focusing in the middle of the LHM flat lens as well as a refocus were observed in the second PPW.

### 5.3 Parabolic lens

Fig. 13 shows the simulation schematic of a parabolic LHM-based lens consisting of 410 mushroom unit-cell structures. An excitation line source is placed inside the PPW and 32.5 mm away from the parabolic interface, corresponding to the parabola's geometric focal point. A PMC wall is placed at the centre of the structure to reduce it to a half simulation space. A total 126 × 220 × 16 FDTD grids have been used, and 150 thousand time steps are calculated. The CFS-PML is also necessary for this case. The equation of parabolic interface is given by $x^2 = 4\,cy$, where $c = 30$ mm is the geometric focus of the parabola. Fig. 14 is the $E_z$-field distribution above the substrate when the frequency is 3.77 GHz.

A parabolic LHM-based lens structure was also fabricated and tested based on the schematic in Fig. 13. Fig. 15 shows the measurement results in the area corresponding to the dashed-line region in Fig. 13 at a frequency of 3.77 GHz. In both simulation and measurement, a planar wavefront is observed in the LHM. These results reveal the ability of wave transformation by an LHM-based lens from cylindrical waves to planar waves. The locations of the mushroom structure and PPW are exchanged to show clearer planar wave propagations in Fig. 16. Fig. 16 exhibits the time-domain field distributions of the parabolic lens inside the substrate. A sinusoidal waveform is applied as the excitation source. With the increase of time steps, the planar waves in PPW are generated by the RH/LH interface.

## 6 Conclusion

In this paper, an FDTD method with thin-wire and thin-slot algorithms is proposed and was used to efficiently simulate huge periodic structures. Simulation results using this method were compared to measurement results of an NRI flat lens and parabolic lens based on CRLH mushroom-structure unit cells. Both results show clear LH propagation characteristics at the expected frequency. The PBCs have been utilised to characterise infinite 2D mushroom structures by simulating a single unit mushroom cell. The calculation of the phase of *S*-parameter can be used to verify with PBCs' result for 1D mushroom structures. Comparisons of numerical and experimental results demonstrate the good reliability of the proposed method.

## 7 References


1 Veselago, V.G.: 'The electrodynamics of substances with simultaneously negative values of $\varepsilon$ and $\mu$', *Sov. Phys. Uspekhi*, 1968, **10**, (4), pp. 509–514

2 Caloz, C., Lai, A., and Itoh, T.: 'Wave interactions in a left-handed mushroom structure'. IEEE AP-S/URSI Int. Symp. Dig, July 2004, pp. 1403–1406

3 Sanada, A., Caloz, C., and Itoh, T.: 'Planar distributed structures with negative refractive index', *IEEE Trans. Microw. Theory Tech.,* 2004*,* 52, (4) pp. 1252–1263

4 Lai, A., Wu, W.Y., Leong, K.M.K.H., Itoh, T., and Caloz, C.: 'Quasi-optical manipulations of microwaves using metamaterial interfaces'. IEEE Antenna and Propagation Soc. Int. Symp, July 2005, vol. 1B, pp. 273–276

5 Wu, W.Y., Lai, A., Leong, K.M.K.H., Kuo, C.W., and Itoh, T.: 'Efficient FDTD method for analysis of left-handed mushroom structure'. IEEE Antenna and Propagation Soc. Int. Symp., July 2005, vol. 3A, pp. 798–801

6 Sievenpiper, D., Zhang, L., Broas, F.J., Alexopulos, N.G., and Yablonovitch, E.: 'High-impedance electromagnetic surfaces with a forbidden frequency band', *IEEE Trans. Microw. Theory Tech.*, 1999, **47**, (11), pp. 2059–2074

7 Elek, F., and Eleftheriades, G.V.: 'Dispersion analysis of the shielded sievenpiper structure using multiconductor transmission-line theory', *IEEE Microw. Wirel. Comp. Lett.*, 2004, **14**, (5), pp. 219–221

8 Kokkinos, T., Islam, R., Sarris, C.D., and Eleftheriades, G.V.: 'Rigorous analysis of negative refractive index metamaterials using FDTD with embedded lumped elements'. IEEE MTT-S Int. Microwave Symp. Dig, June 2004, vol. 3, pp. 1783–1786

9 Ziolkowski, R.W., and Heyman, E.: 'Wave propagation in media having negative permittivity and permeability', *Phys. Rev. E*, 2001, **64**, p. 056625

10 Correia, D., and Jin, J.M.: 'Theoretical analysis of left-handed metamaterials using FDTD-PML method'. Microwave Optoelectronics Conf., September 2003, vol. 2, pp. 1033–1036

11 Yee, K.S.: 'Numerical solution of initial boundary value problems involving Maxwell's equation in isotropic media', *IEEE Trans. Antennas Propag.*, 1966, **14**, (3), pp. 300–307

12 Taflove, A., and Hagness, S.C.: 'Computational electrodynamics: the finite-difference time-domain method' (Artech House, Boston, MA, 2000, 2nd edn.)

13 Mäkinen, R.M., and Kivikoski, M.A.: 'A stabilized resistive voltage source for FDTD thin-wire models', *IEEE Trans. Antennas Propag.*, 2003, **51**, (7), pp. 1615–1622

14 Gilbert, J., and Holland, R.: 'Implementation of the thin-slot formalism in the finite-difference BMP code THREDII', *IEEE Trans. Nucl. Sci.*, 1981, **28**, pp. 4269–4274

15 Gkatzianas, M.A., Balanis, C.A., and Diaz, R.E.: 'The Gilnert–Holland FDTD thin slot model revisited: an alternative expression for the in-cell capacitance', *IEEE Microw. Wirel. Comp. Lett.*, 2004, **14**, (5), pp. 219–221

16 Shlager, K.L., and Schneider, J.B.: 'Relative accuracy of several finite-difference time-domain schemes'. IEEE AP-S/URSI Int. Symp. Dig., July 1999, vol. 1, pp. 168–171

17 Berenger, J.P.: 'A perfectly matched layer for the absorption of electromagnetics waves', *J. Comput. Phys.*, 1994, **114**, (2), pp. 185–200

18 Harms, P., Mittra, R., and Ko, W.: 'Implementation of the periodic boundary condition in the finite-difference time-domain algorithm for FSS structures', *IEEE Trans. Antennas Propag.*, 1994, **42**, (9), pp. 1317–1324

19 Turner, G., and Christodoulou, C.: 'Broadband periodic boundary condition for FDTD analysis of phased array antennas'. IEEE Antenna and Propagation Soc. Int. Symp, June 1998, vol. 2, pp. 1020–1023

20 Schurig, D., and Smith, D.R.: 'Universal description of spherical aberration free lenses composed of positive or negative index media' ArXiv Physics e-Prints, July 2003, 0307088,

21 Roden, J.A., and Gedney, S.D.: 'Convolution PML (CPML): an efficient FDTD implementation of the CFS-PML for arbitrary media', *Microw. Opt. Tech. Lett.*, 2000, **27**, (5), pp. 334–339

22 Bécache, E., Petropoulos, P.G., and Gedney, S.D.: 'On the long-time behavior of unsplit perfectly matched layers', *IEEE Trans. Antennas Propagat.*, 2004, **52**, (5), pp. 1335–1342